

STUDY OF THE  
THERMODYNAMIC NATURE  
OF THE DISORDER-DRIVEN  
VORTEX MATTER PHASE  
TRANSITION

By

Nurit Avraham

*Thesis for the M.Sc. degree submitted to  
the Scientific Council of the Weizmann  
Institute of Science*

December 2000

Carried out under the supervision  
of  
Professor Eli Zeldov

Weizmann Institute of Science

Abstract

STUDY OF THE THERMODYNAMIC  
NATURE OF THE DISORDER-DRIVEN  
VORTEX MATTER PHASE TRANSITION

By Nurit Avraham

Vortex matter in high-temperature superconductors (HTSC) has a rich and complicated phase diagram. The nature of the different vortex matter phases and the transitions between them are the subject of intense theoretical and experimental investigations. It is generally accepted that at high temperatures the relatively ordered vortex lattice melts through a *thermally induced* first-order transition (FOT) into a vortex liquid phase, whereas at low temperatures the ordered vortex lattice transforms into a disordered vortex phase through a *disorder-driven* transition, which is characterized by the second magnetization peak. It was proposed that the first-order melting line terminates at a critical point  $T_\phi$  that defines the crossover from the FOT to the second peak regime.

While the high temperature region of the phase diagram has been extensively studied, at low and intermediate temperatures the investigation of the equilibrium vortex state is difficult, due to pinning of vortices by material disorder. Hence, one of the major open questions in the phase diagram of HTSC is the thermodynamic nature of the disorder-driven transition. Another important issue that is not well understood is the flattening of the melting line near the crossover to the disorder-driven transition and the termination of the melting line at the critical point.

In this research work we have investigated the phase diagram of  $\text{Bi}_2\text{Sr}_2\text{CaCu}_2\text{O}_8$  (BSCCO) crystals at low temperatures. We have focused on the critical point and on the behavior of the melting line in the vicinity of  $T_\phi$  as well as on the thermodynamic nature of the disorder-driven transition. In particular we addressed the question whether this transition is of a first-order or a continuous nature. In order to overcome the difficulties arising from the non-equilibrium conditions of low temperatures, we implemented a recently introduced “shaking” technique, using an in-plan AC magnetic field. This technique was found to equilibrate the vortex lattice in BSCCO superconductors at low temperatures, enabling the observation of equilibrium vortex properties.

As a result, we have found that the FOT extends beyond the critical point, which implies that the previously reported termination of the FOT at  $T_\phi$  does not reflect a real critical point, but rather an experimental limitation. The extended first-order transition line was found to coincide with the disorder-driven transition, resulting in a unified FOT that gradually changes its character from a thermal melting at high temperatures to a disorder induced transition at low temperatures. At intermediate temperatures, this transition was found to display an unusual inverse melting behavior, where a disordered vortex phase transforms into an ordered lattice with increasing temperature. Paradoxically, the structurally ordered lattice has larger entropy than the disordered phase.

## TABLE OF CONTENTS

|   |    |
|---|----|
| Introduction.....   | 1  |
| Scientific Background .....                                   | 3  |
| Superconductivity – The Basic Phenomena.....                  | 3  |
| The Ginzburg-Landau Theory and the Mixed State.....           | 4  |
| Vortex Matter in High- $T_c$ Superconductors.....             | 8  |
| The Phase Diagram of BSCCO Crystals.....                      | 11 |
| Methodology.....  | 14 |
| Hall Sensor Measurements.....                                 | 14 |
| The In-plane AC Field.....                                    | 15 |
| Experimental Setup.....                                       | 16 |
| The Cryogenic System .....                                    | 16 |
| The Hall Sensor Array .....                                   | 17 |
| The In-plane AC Field.....                                    | 18 |
| Results And Discussion.....                                   | 20 |
| Eliminating Irreversibility Using the In-plane AC Field ..... | 20 |
| The Thermodynamic Nature of the Phase Transitions.....        | 22 |
| Inverse Melting.....  | 26 |
| Summary.....  | 29 |

## ACKNOWLEDGMENTS

I am most grateful to my supervisor, Prof. E. Zeldov, for making the past year so exciting and stimulating, for his advice and support, and for sharing his knowledge and experience with me.

Special thanks to Dr. Y. Myasoedov for his patient assistance, to Dr. M. Rapaport, Dr. H. Shtrikman, and to my friends and colleagues Mr. Y. Paltiel, and Mr. A. Soibel.

## *Chapter 1*

### INTRODUCTION

The discovery of high-temperature superconductors (HTSC) in 1986 [1] renewed the interest in superconductors. These materials are Type II superconductors, in which external magnetic fields penetrate the material in the form of magnetic flux lines – vortices – forming a mixed state. The behavior of vortices, under various temperature and magnetic field conditions, is interesting both from the practical and scientific point of view.

From the practical point of view, the design and performance of superconductor-based applications is often limited by the suppression of superconductivity at intense magnetic fields. In the mixed state, resistance to current flow can occur since the vortices tend to move in the presence of applied currents due to the Lorentz force. This motion of vortices perpendicular to the current produces energy dissipation and an effective resistance in the superconductor appears. Knowing how the vortices move and arrange themselves under various temperature and magnetic field conditions will be critical in controlling the phenomena and in maintaining a dissipationless current.

From the scientific point of view, the vortex matter system is very attractive as it provides a remarkable example of a condensed matter state with tunable parameters [2], enabling the study of general phase transition behavior. Experimentally, all the relevant parameters can be varied over wide ranges - the vortex density can be changed by varying the external magnetic field, thermal fluctuation can be changed by varying the temperature, quenched disorder can be modified through controlled irradiation, and the coupling energy between the  $\text{CuO}_2$  layers can be altered through the choice of material. The vortex matter in HTSC exhibits a very complicated phase diagram consisting of a variety of liquid and solid phases and transitions among them - some of which are still not well understood.

In this work, we used a local Hall sensors array technique [3,4] - combined with a recently introduced vortex “shaking” technique [5] - to present a study of the low temperature region of the phase diagram of the vortex matter in the  $\text{Bi}_2\text{Sr}_2\text{CaCu}_2\text{O}_8$  (BSCCO) HTSC.

BSCCO is a layered high-temperature superconductor with a  $T_c$  of  $\approx 90$  K and a very high anisotropy ratio [6].

This work is divided as follows:

- The scientific background, briefly describing the basic phenomena and theory of superconductivity relevant to this work, is described in chapter 2.
- The methodology of, and the motivation for, the specific experimental techniques are given in chapter 3.
- Chapter 4 provides the description of the experimental setup.
- Presentation and discussion of experimental results are provided in chapter 5.
- Chapter 6 summarizes the results.

## Chapter 2

### SCIENTIFIC BACKGROUND

#### Superconductivity – The Basic Phenomena

The electrical resistance of many metals and alloys vanishes abruptly when they are cooled below a certain temperature  $T_c$ , which is a characteristic of the material. This phenomenon of superconductivity was discovered by Kamerlingh Onnes[7] in Leiden in 1911, three years after he first liquefied Helium. At the critical temperature  $T_c$ , the material undergoes a phase transition from a state of normal electrical resistivity to a superconducting state. It was immediately recognized that this phenomenon is of vast potential importance in technology because it means that current can flow through a superconducting material without any losses. Current induced in a superconducting ring, for example, has been demonstrated to persist for several years without any diminution – where no battery of any kind was present. Thus, *perfect conductivity* is the first important property of superconductivity. Another important property of superconductivity is *perfect diamagnetism*. In 1933 two German physicists, Meissner and Ochenfeld [8], found that superconductors expel magnetic fields: if a superconductor in its normal state is put in a magnetic field, and the temperature is lowered below the critical temperature (where the material becomes a superconductor) the magnetic field is expelled. The way in which this process takes place divides the superconducting materials into two types – Type I and Type II. Fig. 1 shows the  $H$ - $T$  phase diagram of the two types. In Type I materials (Fig. 1a) the magnetic field is totally excluded from the material up to a critical field  $H_c$  and above  $H_c$  the magnetic field penetrates completely into the sample and normal electrical resistance is restored. Thus, below  $H_c$  the material is in its superconducting state (Meissner state), and above  $H_c$  the material is in its normal state. In Type II materials (Fig. 1b), the perfect superconducting state with a total expulsion of the magnetic field exists up to a lower critical field  $H_{c1}$ . At fields above the upper critical field  $H_{c2}$  the magnetic field penetrates completely, and the material is in its normal state. In the intermediate region between  $H_{c1}$  and  $H_{c2}$  there is a *mixed state* at which the magnetic field penetrates into the superconductor in the form of quantized flux lines, or vortices.

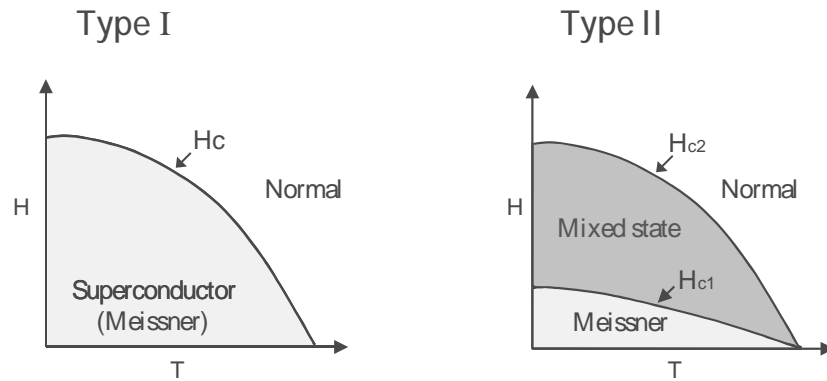


Fig. 1 H-T phase diagrams of Type I and Type II superconductors

### The Ginzburg-Landau Theory and the Mixed State

The Ginzburg-Landau (G-L) theory [9,10] is a phenomenological theory, which explains rather well the behavior of superconductors in an applied magnetic field. Although it is based on the free energy expansion near  $T_c$ , its main results remain valid in the entire range of temperatures.

It is based on three fundamental assumptions:

1. There exist an order parameter  $\psi$ , which goes to zero at the transition
2. The free energy may be expanded in powers of  $\psi$
3. The coefficients are regular functions of  $T$

The expansion of the G-L free energy density, when  $\psi$  is a complex nonlocal variable, is given by:

$$f = f_{n0} + a|\psi|^2 + \frac{b}{2}|\psi|^4 + \frac{1}{4m} \left| \left( \frac{\hbar}{i} \nabla - \frac{2e}{c} \vec{A} \right) \psi \right|^2 + \frac{H^2}{8\mu_0} \quad (1)$$

Here  $f_{n0}$  is the free energy density of the normal state at zero magnetic field;  $a$  and  $b$  are parameters depending on the temperature and the material;  $m$  and  $e$  are the mass and the charge of the electron respectively;  $\vec{A}$  is the magnetic field vector potential; and  $H$  the external magnetic field.

Integrating equation (1) over the sample volume gives the free energy, and by minimizing it, we get the two G-L equations:

**Error! Objects cannot be created from editing field codes.** (2)

**Error! Objects cannot be created from editing field codes.** (3)

Equation (2) gives the variation of  $Y$  once we know the vector potential  $\bar{A}$ , while equation (3) gives the distribution of the current.

The two Ginzburg-Landau equations have two special solutions:

$Y = 0$  where  $\bar{A}$  is determined only by  $H = \text{curl}\bar{A}$ . This solution describes the normal state.

$Y = Y_0 = (-a/b)^{1/2}$  and  $\bar{A} = 0$ , this solution describes the ordinary superconductor state, with perfect Meissner state.

There are two characteristic lengths, which can be deduced from the equations in the limit of weak magnetic fields. From equation (2) we can obtain the coherence length

$\xi(T) = \frac{-\hbar^2}{2ma}$ , which characterizes the distance over which  $\psi(\mathbf{r})$  decreases to zero. From

equation (3) we can obtain the penetration depth  $\lambda(T) = \left[ \frac{mc^2}{16pe^2Y_0^2} \right]^{1/2}$ , which

characterizes the distance of penetration of the magnetic field into a superconducting region. The ratio of these two characteristic lengths defines the G-L parameter  $k = \frac{\lambda}{\xi}$ ,

which differentiates between the two types of superconductors.

The significance of  $k$  becomes clearer if we look at the surface energy of the interface between the superconducting and normal phases. For the boundary to be in equilibrium, the Gibbs free energy on each side must be the same. Consider the change in energy in going from the superconducting to the normal side of the boundary. The change is not abrupt since  $\psi$  decreases to zero over a distance  $\xi(T)$ . Hence, we pay an energetic cost of

$\sim \frac{H_c^2}{8p} \xi$  per unit area because of loss of condensation energy on a scale  $\xi$ . On the other

hand we reduce the magnetization energy by  $\sim \frac{H_c^2}{8p} \lambda$  per unit area, since the magnetic

field penetrates a distance  $\lambda(T)$  into the superconducting phase. Thus the surface energy per

unit area is  $E_{surf} \sim \frac{H_c^2}{8\rho}(x - 1)$ . Meaning that for  $k \ll 1$  the surface energy is positive, whereas for  $k \gg 1$  the surface energy is negative. A precise calculation within the framework of the G-L theory [11] shows that the surface energy changes sign at  $k = \frac{1}{\sqrt{2}}$ . The situation is therefore such that for  $k < \frac{1}{\sqrt{2}}$  we have a positive surface energy with Type I behavior, whereas for  $k > \frac{1}{\sqrt{2}}$  the surface energy is negative resulting in Type II behavior.

The behavior of Type II superconductors can be described in terms of surface energy. The appearance of a normal region in the superconducting region lowers the Gibbs free energy so that it may be energetically favorable for the material to split up into a large number of small normal filaments to produce a maximum boundary area relative to the volume of the normal material. This is the situation in the mixed state, where the magnetic field penetrates the sample in the form of small normal filaments, or vortices. The structure of an individual vortex (Fig. 2) depends on the coherence length and penetration depth. The vortex has a normal core whose radius is the coherence length. The normal core is surrounded by supercurrents that produce magnetic field. Thus, in the middle of the normal core, the magnetic field has its highest value, and it decays exponentially with a characteristic length  $\lambda$ . The total magnetic flux each vortex contains is exactly one quantum of magnetic flux  $f_0 = \frac{hc}{2e} = 2.07 \times 10^{-7} G \cdot cm^2$ . The vortices repel each other and hence spread out over the entire sample volume and form a regular array, known as the Abrikosov vortex lattice.

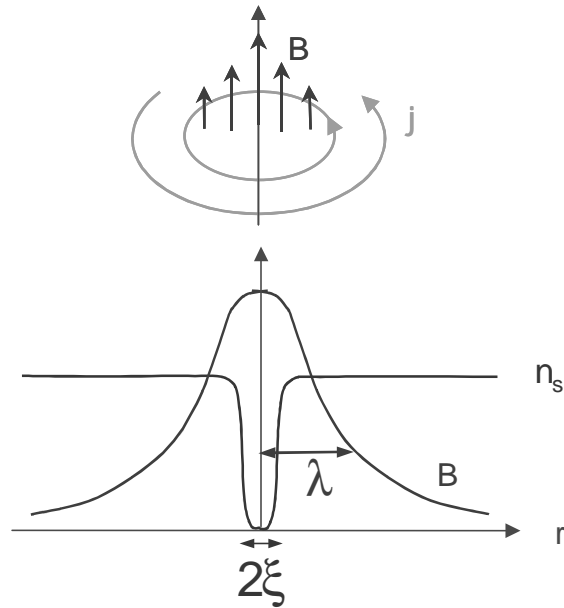


Fig. 2 Structure of one vortex line in a Type II superconductor. The vortex line is surrounded by a current loop. The magnetic field  $B$  is at its maximum near the center of the line. Going outwards,  $B$  decreases to zero with characteristic length  $\lambda$ . The density of superconducting electrons,  $n_s$ , is reduced only in a small "core region" of radius  $\xi$ .

The mixed state of Type II superconductors was derived by Abrikosov in 1957 [12,13]. Based on the Ginzburg-Landau theory, he predicted that the magnetic field in Type II superconductors would penetrate the sample as quantum flux lines that form a hexagonal array called the vortex lattice. This vortex lattice has been observed using different techniques such as magnetic decoration [14], neutron scattering [15,16], electron microscopy [17], electron holography [18], and Hall probe microscopy [19].

The behavior of the magnetic vortices constituting the mixed state is intimately related to the most important practical defining characteristic of the superconducting state: its ability to carry an electrical current without loss. The central idea is that the moving vortices dissipate energy. When an applied current flows through a superconductor in its mixed state, there is a Lorentz force between the current and the magnetic flux lines. The force on a single line is given by the expression  $F = J \times f_0$  [20], where  $J$  is the transport current density, and  $\Phi_0$  is a vector of magnitude  $\frac{h^2 c^2}{4\pi e^2}$  directed along the flux line. Because of this force, flux lines tend to move transverse to the current. If the vortices move with velocity

$V$ , they induce an electric field of magnitude  $E = B \times \frac{V}{c}$  (due to the Lorentz transformation), which is parallel to  $J$ . This acts as a resistive voltage, and power is dissipated. (The energy dissipation per unit time per unit volume is  $E \cdot J$ ). This means that an ideal superconductor in its mixed state does not display perfect conductivity. Thus, in order to achieve zero resistivity in a Type II superconductor in its mixed state, we should prevent all vortices from moving. This actually does happen at low enough temperatures, because vortices are pinned by imperfections in the material.

### **Vortex Matter in High- $T_c$ Superconductors**

In 1986, Bednorz and Müller [1], from the IBM Zurich Research Center, discovered a new class of Type II superconductors. These materials, a family of copper oxide ceramics, were found in some cases to superconduct at a temperature that exceeded 140 Kelvin. This discovery was surprising and exciting not only because of the large increase in  $T_c$  but also because these materials can easily be cooled by liquid Nitrogen instead of liquid Helium – which implies economical advantages. Soon after the discovery of the copper oxide high-temperature superconductors, it was shown that the resistivity in the temperature and magnetic field regime where the Abrikosov lattice was expected to form, behaves in a qualitatively different fashion from that found in previously studied Type II superconductors [21]. The reason for the difference is that strong thermal fluctuations cause the vortex lattice to melt into a vortex liquid well below the upper critical field  $H_{c2}$ . The reason for the strong thermal fluctuations in HTSC is the combination of high operating temperatures, short superconducting coherence length, long penetration depth, and high anisotropy [22]. These materials are built of superconducting  $\text{CuO}_2$  planes coupled by Josephson tunneling between adjacent layers and separated by blocking layers of normal metallic or insulating materials that act as potential barriers against the tunneling of super-electrons between planes. If the coupling between layers is weak compared to thermal energies, the vortex lines behave more like strings of points or “pancake” vortices in each superconducting layer, with only rather weak correlation between vortices in different layers. Therefore, the weak coupling between the layers leads to highly flexible vortices with anisotropies  $m_z/m_{\perp}$  of 100,000 or more. (Compared to anisotropies of 1 in conventional superconductors.)

In the absence of thermal fluctuations and of pinning induced disorder (which will be discussed later), the vortex lattice is present at all fields below  $H_{c2}$ . However, in the presence of strong thermal fluctuations the vortex lines in the lattice vibrate with larger amplitudes as the temperature rises. At sufficiently high temperatures, the lines vibrate enough to cause melting of the vortex lattice. Actually, there is a competition between the repulsive interaction between the vortices, which stabilizes them into a regular lattice, and the thermal energy. The melting transition occurs when the energy of thermal fluctuations becomes equal to the elastic energy barriers keeping vortices near their equilibrium positions in the lattice [23]. Theoretically, it is expected that this transition would occur by way of a first-order transition in clean systems [24], with a gradual transition in systems with quenched disorder [2]. Extensive experimental studies, including transport [25,26], magnetization [27], AC susceptibility [28], and calorimetric methods [29] confirmed the existence of such a first-order transition in relatively clean  $\text{YBa}_2\text{Cu}_3\text{O}_7$  (YBCO) and BSCCO crystals. Figure 3 shows a schematic phase diagram of high-temperature superconductors.

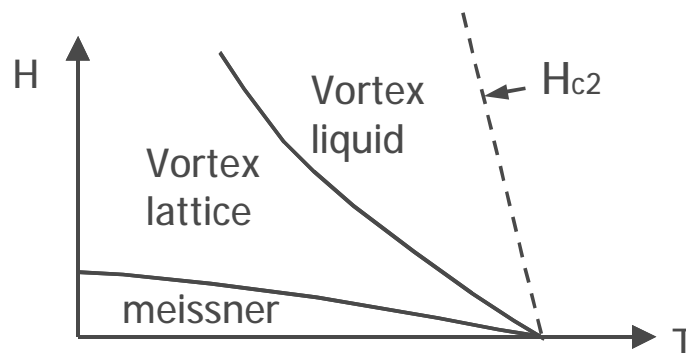


Fig. 3 Schematic phase diagram of HTSC. The vortex solid is either a lattice (for clean superconductors) or a glass (for dirty ones).

In perfectly clean and ideal material, the vortex liquid freezes into a regular lattice on decreasing the temperature. However, real materials always have chemical and structural imperfections. When such materials are cooled to below the melting temperature, the vortices are pinned by material imperfections, since it is energetically favorable. This pinning disrupts the regular lattice pattern that would otherwise form in ideal and pure materials. There are two competing effects: the repulsive interaction between the vortices

favors a lattice structure, but the randomly located material defects tend to pin the lines at random positions, disrupting the lattice structure. Thus, random pinning turns the vortex lattice phase into a vortex glass phase [30]. Further investigations [31-33] in the presence of disorder reveal even more complicated phase diagrams. The results suggest the existence of at least two distinct glass phases in the presence of quenched disorder. At low fields where elastic interaction dominates, the vortex lattice is only *weakly* destroyed, resulting in a quasilattice phase in which a relatively well-defined lattice structure is observed. This phase was recently termed Bragg glass [34] in which there are no dislocations in the lattice. At higher fields, where the pinning energy dominates, the vortex lattice is *dramatically* destroyed resulting in an entangled solid phase where elementary cells of vortex lattice are twisted and dislocations proliferate [23,36] (Fig. 4).

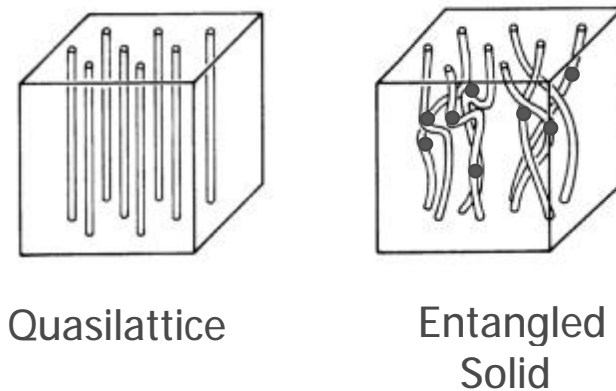


Fig. 4 Two kinds of vortex solid: a relatively ordered quasilattice and a highly disordered entangled solid

To summarize, this rich equilibrium behavior of vortex matter in HTSC arises from the competition of four energies:

- Vortex interaction energy favors a perfect vortex lattice
- Thermal energy favors the vortex liquid state
- Pinning energy favors the glassy solid state
- Coupling energy determines the flexibility of the flux line. The melting temperature depends dramatically on the flexibility of the lines. In materials with weak coupling

and thus highly flexible vortices, the melting line resides at much lower temperatures than in materials with strong coupling.

HTSCs have the advantage that all these energies can be of the same order of magnitude, resulting in a variety of liquid and solid phases. Thus, the vortex matter provides a remarkable example of condensed state for exploring general phase transition phenomena [2].

### The Phase Diagram of BSCCO Crystals

One of the high-temperature superconducting materials that displays a rich and complicated phase diagram is  $\text{Bi}_2\text{Sr}_2\text{CaCu}_2\text{O}_8$ , a layered high  $T_c$  superconductor with a  $T_c$  of about 90 K and a very high anisotropy ratio [6].

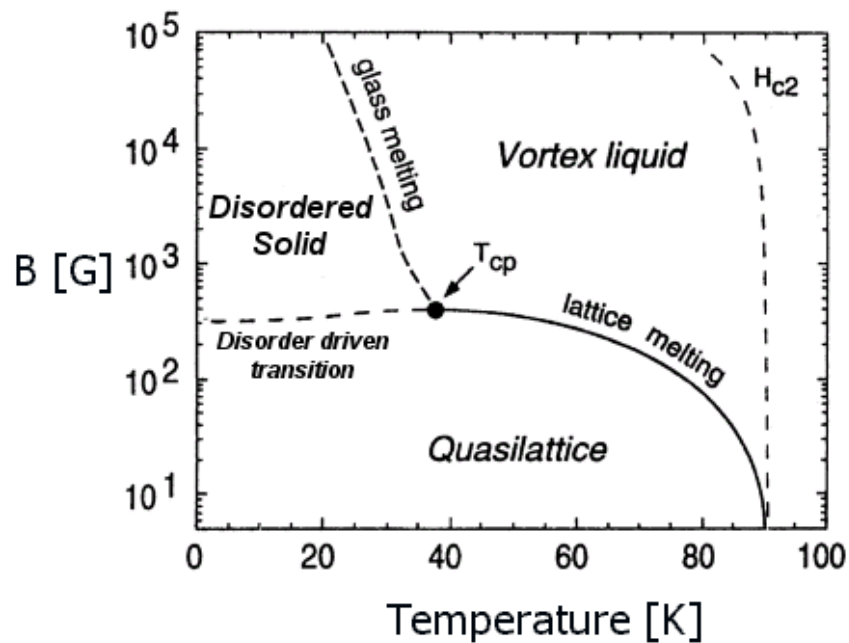


Fig. 5 Schematic phase diagram (on logarithmic scale) of a highly anisotropic HTSC in the mixed state based on experimental results in BSCCO. A major part of the phase diagram is occupied by a vortex liquid phase. The quasilattice state is a rather ordered solid state at which the elastic energy dominates. The disordered solid is a highly disordered vortex phase where the pinning energy dominates. At elevated temperatures, the quasilattice is destroyed by thermally induced first-order melting transition. At low temperatures, the quasilattice is destroyed by a disorder-driven transition. The glass melting is a line at which the enhanced pinning tends to vanish. It is still unknown whether this line represents a crossover or a thermodynamic transition.

Figure 5 shows a schematic phase diagram of HTSC based on experimental results in BSCCO [23, 32]. There are three main vortex phases: a relatively ordered **quasilattice** at low fields, a **highly disordered vortex solid** at higher fields, and a **vortex liquid** at high temperatures.

At high temperatures, the strong thermal fluctuations melt the quasi-lattice into a vortex liquid. This melting transition is a thermodynamic first-order transition [27,29]. A first-order phase transition is associated with a discontinuous step in density. Because each vortex carries a quantum of magnetic flux, a step in the vortex density is identical to a step in the local magnetic field. Hence, this melting transition is characterized by a sharp step in the local magnetic field  $B$  (or in the equilibrium magnetization), as shown in Fig. 6. It was found that this thermally induced FOT line shows a flattening at lower temperatures and terminates at a critical point  $T_\phi$  around 39 K [27,32]. It is still not understood whether this termination of the melting line reflects a real critical point, since at a real critical point the height of the step in the local magnetic field is expected to decrease continuously to zero on approaching  $T_\phi$ , whereas experimentally the step was found to disappear abruptly.

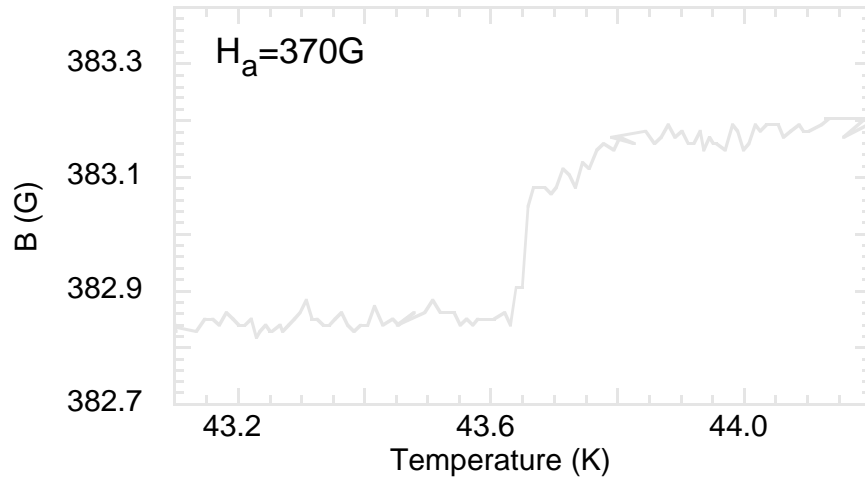


Fig. 6 An example of the step in local  $B$  on crossing the melting line by decreasing the temperature at a constant applied field

At low temperatures, where the disorder plays an important role, the vortex matter undergoes a disorder-driven phase transition from an ordered quasi-lattice to a highly disordered vortex solid [33,37]. With increasing field, the elastic energy of the lattice decreases relative to the pinning energy, leading to a structural transition when the two

energies become comparable. It was found that this transition results in enhanced vortex pinning, i.e. the quasi-lattice at low fields is weakly pinned, whereas the disordered vortex phase at high fields is characterized by a higher critical current [32]. This transition is called the second peak transition, as it manifests itself in the magnetization measurements as a second peak in local magnetization loops (Fig. 7).

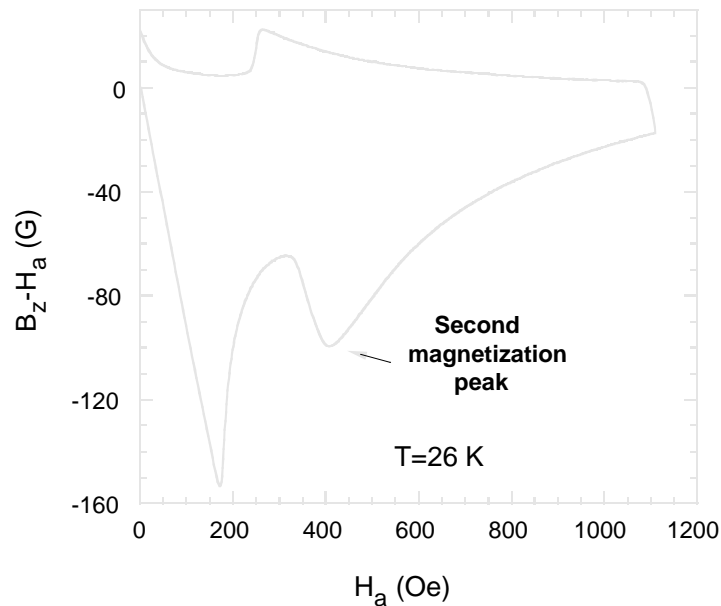


Fig. 7 An example of a second magnetization peak in the local magnetization loop.

It was suggested that these two phase transitions (the melting transition and the second peak transition) form one continuous transition line that changes from a first to a possibly second order transition at a critical point [32], which marks the change from a thermally induced first-order transition to a disorder-driven one. The low and intermediate temperatures of the phase diagram are difficult to study due to the non-equilibrium conditions, caused by vortex pinning, characterizing these regions.

In this work, we investigated the low temperature region of the phase diagram by using a “shaking” technique in order to eliminate the non-equilibrium conditions, trying to understand the thermodynamic nature of the disorder-driven transition, the general temperature dependence of the first-order transition, and its termination at a critical point.

## Chapter 3

### METHODOLOGY

#### Hall Sensor Measurements

The understanding of vortex dynamics in HTSC is based largely on the results of magnetization measurements, in which the magnetic response to an externally applied field is measured. DC magnetization measurements are usually either field sweeps, where the temperature is kept constant and the magnetic field is swept, or temperature sweeps, in which the magnetic field is kept constant. Features in the measurements reveal the different vortex states.

Most of the magnetization measurements are global measurements, in which the integrated magnetic response of the entire sample is measured by magnetic sensors (e.g. SQUID). Some modeling has to be used in order to interpret the resulting magnetization loops since demagnetization effects, bulk currents, surface currents, and the inhomogeneity of the magnetic field inside the sample have to be taken into consideration in the analysis. Moreover, phenomena like vortex matter phase transitions depend on the local value of the magnetic induction inside the sample. Because of the large gradient of the induction present inside the sample, these phenomena are smeared in the global measurements and may even be unnoticeable. Thus, even the most sensitive global measurement techniques are limited in revealing the fine details of vortex dynamics.

In this work, we use a *local* Hall sensor array technique that was developed in our lab [4]. This technique uses an array of two-dimensional electron gas (2DEG) Hall sensors, manufactured using well-established photolithographic and etching techniques. These sensors, which can be manufactured with small dimensions of down to  $1 \times 1 \mu\text{m}^2$ , have the advantage of a linear response to a magnetic field, weak temperature dependence, and high sensitivity. In this technique, the local magnetic induction at the surface of the sample is measured. This quantity is a direct measurement of the density of the vortices inside the sample, since each vortex carries a quantum of magnetic flux. Thus, no a priori model is

needed for the interpretation of the data. The Hall sensor array allows the study of local vortex behavior with high field sensitivity and high spatial resolution so that the real width and height of a transition in the vortex matter can be measured. Furthermore, they enable measurement of the magnetic field just outside the sample's edge – which is very different from the applied magnetic field  $H_a$ , due to the large demagnetization factor of most HTSC samples that are platelet shaped.

### **The In-plane AC Field**

One of the major obstacles encountered when trying to study the behavior of the vortex matter at low temperatures is the formation of non-equilibrium states, which conceal the thermodynamic phase transitions. In such non-equilibrium conditions, the sample shows an irreversible magnetization curve, i.e. the curves on increasing and decreasing fields differ appreciably. In order for a sample to show a reversible magnetization curve, the flux lines must be able to move freely through the sample in order to reach an equilibrium at every value of the applied magnetic field. However, whenever there is vortex pinning, the magnetization curves show some irreversibility. This irreversibility can be explained by the Bean model [35]. If an external field is applied to a slab the vortices enter the surface region until their density closely equals the external flux density. If there is no pinning they spread into the material resulting in a uniform flux density. In the presence of pinning, however, a gradient in vortex density is formed, which is determined by the value of the critical current density. Upon decreasing the external field, the exit of the vortices from the sample is impeded by pinning and a vortex gradient is formed in the opposite direction.

At low temperatures, the effect of pinning by material disorder becomes more significant, thereby preventing the observation of the vortex system in equilibrium due to strong irreversible (or hysteretic) behavior. In order to eliminate this irreversibility, thus restoring equilibrium conditions, we implemented a “shaking” technique [5] in which an additional AC field is applied perpendicular to the constantly applied magnetic field. This technique was found to eliminate the hysteretic behavior and to enable investigation of the vortex matter close to equilibrium conditions.

## *Chapter 4*

### EXPERIMENTAL SETUP

#### **The Cryogenic System**

The cryogenic system is composed of a liquid Helium flow cryostat for temperature stabilization and a superconducting magnet, all inside a 110 liter Helium storage dewar with a 3 inch wide neck. The cryostat, shown in Fig. 8, is a homemade double wall vessel with a needle valve enabling controlled flow of liquid Helium into the sample space. (The walls of the cryostat are vacuum pumped before cooling it in order to achieve thermal isolation.) The flow of the Helium is facilitated by the extra pressure generated naturally within the dewar, which is maintained at about 5 PSI by a pressure valve. Helium leaving the system is constantly collected by our Helium recovery tubing connected to the Helium liquefying station. The cryostat was used for temperature ranges of 4.2 K to 100 K.

Temperature stabilization is achieved by careful control of the flow and the temperature of the gas entering the sample space. The flow is controlled externally by a flow meter, and internally through the needle valve mentioned above. The temperature is measured and stabilized in close proximity to the sample and at the heat exchanger copper block, where the gas enters the cryostat, using two temperature controllers. In this way, most of the high power heating is done before the gas reaches the sample's vicinity, and only sensitive low power stabilization is done near the sample. The temperature sensors used were Lakeshore TG-120PL GaAs diodes that were factory calibrated. The diodes cover a 1.4 K-500 K range, have low magnetic field dependence, and require no periodic recalibration. The 25  $\Omega$  heaters were wound from NiCu 5 mil wires. For temperature control, we used the Lakeshore 330 and the Lakeshore 340 temperature controllers.

The cryostat is surrounded by a superconducting magnet immersed in liquid Helium in the dewar. The magnet (with a current response of 1300 G/A) is a hollow coil surrounding the bottom part of the cryostat, and generates a uniform magnetic field at the location of the sample, and perpendicular to its surface (vertical direction in Fig. 8). Sample mounting and

electrical connections to the measuring apparatus were done using a sample rod. The central body of the rod is a  $\frac{3}{4}$ " diameter stainless steel tube. At the bottom side of the rod is the 24-pin socket accepting a 24-pin chip carrier connected to the Hall sensors array on which the sample is mounted. Also at the bottom of the rod are the temperature sensor and the heater for temperature control, which are covered by a protective cover. A small homemade Helmholtz transverse coil is installed on the protective cover. This coil generates a transverse AC magnetic field. The Hall sensors, the temperature sensors and the AC coil are connected to the connectors at the top of the rod, using Teflon coated wires twisted into pairs.

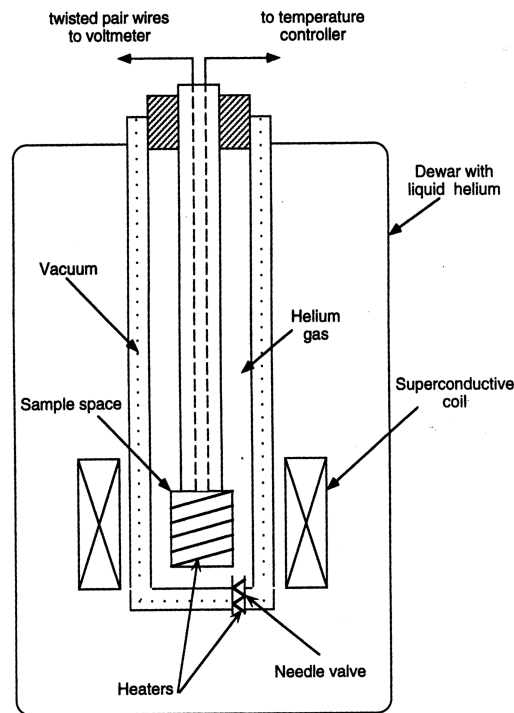


Fig. 8 Schematic drawing of the direct flow cryostat

### The Hall Sensor Array

The experiments were carried out on a number of optimally doped  $\text{Bi}_2\text{Sr}_2\text{CaCu}_2\text{O}_8$  crystals ( $T_c \approx 90$  K) grown in two laboratories [38,39]. The size of the crystals varied from  $100 \times 600 \times 20 \mu\text{m}^3$  to  $700 \times 400 \times 30 \mu\text{m}^3$ . The samples were mounted onto the surface of an array of eleven Hall sensors of  $10 \times 10 \mu\text{m}^2$ , each  $10 \mu\text{m}$  apart (see Fig. 9). The sensors were made from two-dimensional electron gas (2DEG) formed at a GaAs/AlGaAs interface.

The 2DEG active layer resided only  $\approx 1000 \text{ \AA}$  below the surface, resulting in a very accurate measurement of the local magnetic field at each of the sensor locations across the sample. The 2DEG usually has a mobility of about  $1 \times 10^5 \text{ cm}^2/\text{V sec}$  at 80 K and a density of about  $6.25 \times 10^{11} \text{ cm}^{-2}$  resulting in a sensitivity of about  $0.1 \text{ } \Omega/\text{Gauss}$ . In the DC magnetization measurements, a  $50 \text{ } \mu\text{A}$  Hall current was driven through the sensor array and the Hall voltage was measured using a Keithley 182 sensitive digital voltmeter for two opposite polarities of the Hall current. All the sensors in the array were measured one after the other for each temperature and field by switching the voltmeter connection to each sensor, using a Keithley 7001 switch system.

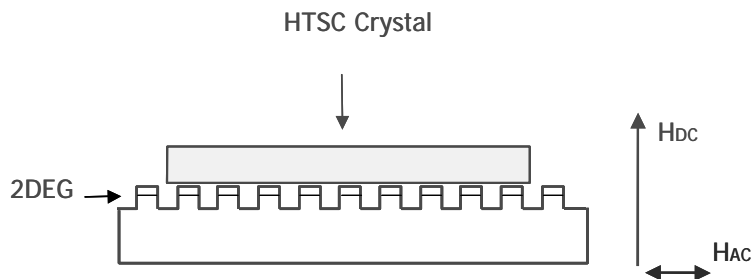


Fig. 9 Schematic side view of BSCCO crystal glued on the surface of the sensors

### The In-plane AC Field

The transverse AC field was generated by a small homemade Helmholtz coil, which was installed on the protective cover of the rod sample, transversely to the superconducting coil axis. It consisted of two circular coaxial coils wound from Cu 1.6 mm wires and with a current response of 80 G/A. The AC field was generated at the location of the sample, parallel to the surface of the sample – along the sensor array (the perpendicular direction was tested, but was found to be less efficient). The perpendicular DC magnetic field and the parallel AC magnetic field were simultaneously applied to the sample. A Copa model PA9000 commercial amplifier, driven by the sine output of an EG&G PARC 5302 lock-in amplifier, was used to create the AC current through the coil.

The efficiency of the vortex shaking depends on the frequency and amplitude of the AC magnetic field. Experimentally, a frequency of 1kHz was found to be optimal. The amplitude of the AC field was varied according to the measurement temperature – AC

RMS current of  $\approx 450$  mA (equivalent to an AC RMS magnetic field of 36 G) was sufficient to eliminate the irreversibility of the magnetization loop at high temperatures above 50 K. At intermediate temperatures, from 50 K down to 38 K, we usually applied AC current of  $\approx 700$  mA and at low temperatures we used our maximum AC current of 1-1.3 A. Above 1.3 A the heat produced by the AC coil prevented a reliable temperature stabilization around the desired temperature.

In most of the measurements the AC magnetic field was applied constantly during the whole field or temperature sweep. To eliminate AC field side effects, an alternative mode was tried: every measurement step was performed in a three-stage cycle – increasing the DC field, applying the AC field for a limited time, and finally taking the measurement. This alternative was found to be very noisy.

To check the reliability of the measurements, a measurement using the additional AC field was compared to a measurement without it.

The entire experiment was controlled by a computer program written in LabView. The input from the measurement apparatus was carried through a GPIB bus (IEEE-488 standard interface).

## Chapter 5

### RESULTS AND DISCUSSION

We present results on three BSCCO crystals with typical dimensions A- $160 \times 600 \times 25 \mu\text{m}^3$ , B- $190 \times 900 \times 30 \mu\text{m}^3$ , and C- $170 \times 600 \times 20 \mu\text{m}^3$ .

#### **Eliminating Irreversibility Using the In-plane AC Field**

As previously mentioned, the observation of the vortex system at equilibrium conditions at low temperatures becomes difficult due to the appearance of irreversibility in the magnetization curve. Willemin et al. [5] have recently shown that in YBCO a transverse AC field reduces the effect of vortex pinning at high temperatures close to  $T_c$ . We found that in BSCCO crystals this method can fully suppress the magnetization hysteresis even at low temperatures down to 30 K, as shown in Fig. 10a. The figure shows two local magnetization loops at  $T=30$  K: a magnetization loop with the additional AC field and one without it. The measurement without the AC field shows a hysteretic magnetization loop, characterized by the second magnetization peak, whereas the measurement with the AC field displays a *fully reversible* magnetization loop curve. Due to the high anisotropy of BSCCO and its layered structure, the in-plane AC field  $H_{ac}$  readily penetrates through the sample in the form of Josephson vortices [40]. The Josephson vortices cause small relative displacements between the pancake vortices in the adjacent  $\text{CuO}_2$  layers. We believe that  $H_{ac}$  induces local “shaking” of the vortices, which reduces pinning and flattens out the sand-pile-like Bean profiles, resulting in reversible magnetization loops. In addition to the bulk pinning, a substantial part of the magnetic hysteresis in BSCCO crystals is caused by surface [41] and geometrical [42] barriers. We found that  $H_{ac}$  also efficiently suppresses this source of hysteresis, probably through instantaneous cutting of the vortices by the Josephson vortices, allowing easy penetration of individual pancake vortices through the sample’s edges.

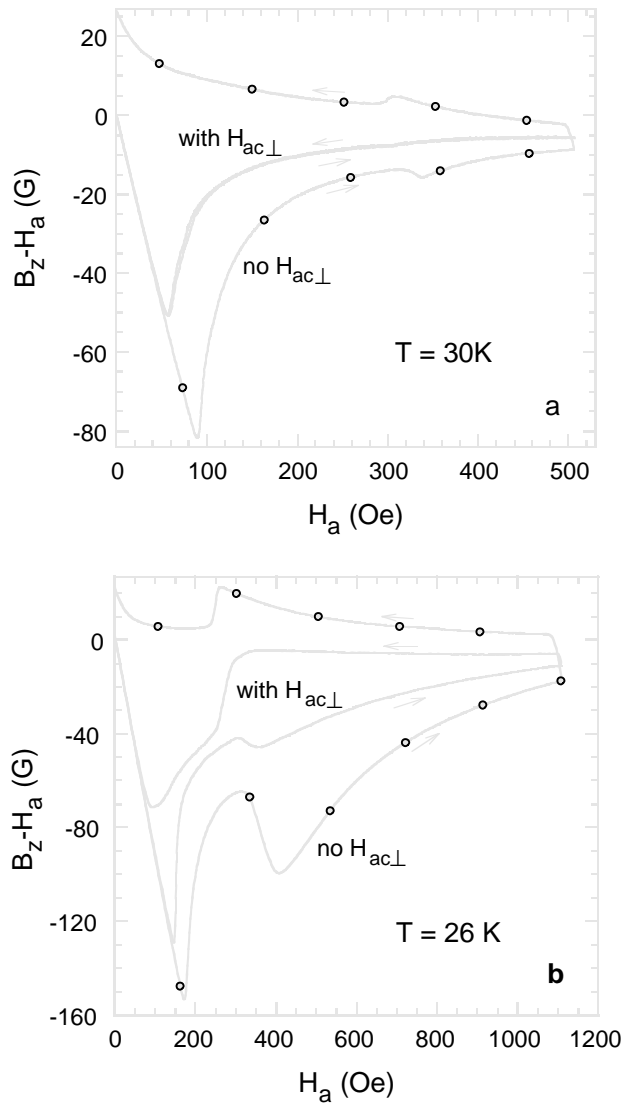


Fig. 10 Local magnetization loops in a BSCCO crystal with and without ( $\circ$ ) transverse AC field  $H_{ac}$ . (a) Crystal A at 30K, the lowest temperature at which a fully reversible magnetization is attained for our maximum  $H_{ac}$  of about 80 G. (b) Crystal C at 26 K, our maximum  $H_{ac}$  was not sufficient to obtain a reversible magnetization.

Fig. 10b shows an example of the magnetization loop at a lower temperature of 26 K. Here, the width of the DC loop is significantly larger than the width at 30 K and our maximum amplitude of  $H_{ac}$  was not sufficient to obtain a reversible magnetization. It is interesting to note that the efficiency of  $H_{ac}$  is different in the two vortex phases. For the same width of the original loop, a much stronger suppression of the hysteresis of the

ordered lattice was observed as compared to the disordered phase above the second magnetization peak. This is probably because this phase exhibits a stronger vortex pinning.

### The Thermodynamic Nature of the Phase Transitions

The most direct way to determine the nature of a phase transition is to observe the discontinuity in the local magnetization loop. At high temperatures, in clean BSCCO crystals, the first-order melting transition manifests itself as a clear and sharp step in the local magnetization curve. However, at lower temperatures this magnetization step was suppressed by the appearance of the irreversibility effect, and disappeared abruptly at a specific temperature that was assumed to be a critical point. Eliminating the irreversibility by  $H_{ac}$  allowed us to observe a magnetization step at temperatures below this critical point.

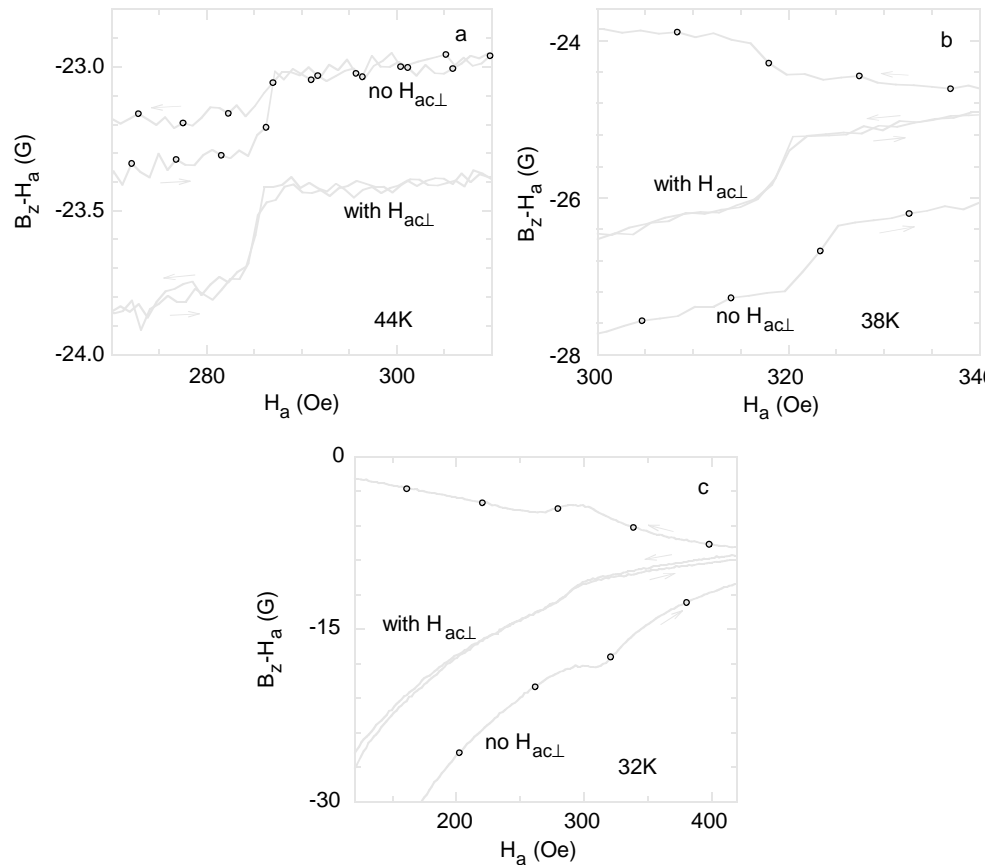


Fig. 11 Local magnetization loops in the vicinity of the melting transition with and without (o) a transverse AC field  $H_{ac}$ . (a) Crystal B at 44K, above the critical point. (b) Crystal B at 38K, just below the critical point. (c) Crystal C at 32K, far below the critical point.

Figure 11 shows local magnetization curves in the vicinity of the first-order melting transition at different temperatures in the presence of the AC field and in the absence of it. At 44 K (Fig. 11a), which is above the  $T_{\varphi}$  of 40 K in this crystal, the magnetization step can still be resolved in the curve measured without the  $H_{ac}$  but is partially suppressed by a hysteresis that develops in the vortex solid just below the transition. Application of  $H_{ac}$  fully removes the hysteresis and enhances the magnetization step, as seen in the curve measured with the  $H_{ac}$ .

Figure 11b demonstrates the behavior at 38 K, just below  $T_{\varphi}$ . At this temperature, the second magnetization peak and a large hysteresis start to develop. The application of  $H_{ac}$  removes the hysteresis and reveals the underlying magnetization step, indicating the first-order nature of the transition.

A similar effect is obtained at 32K – far below the critical point – as shown in Fig. 11c. Here a fully developed second magnetization peak turns into a step in the reversible magnetization loop upon application of  $H_{ac}$ . Note that the magnetization step is much smoother in this figure because this is a different crystal, which displayed a broader step in the whole temperature range.

Some broadening of the magnetization step is apparent in all figures. We attribute this broadening to the fact that a transverse field is known to slightly shift the melting field [43]. Such a small shift during the AC cycle should cause a broadening of the magnetization step.

In contrast to previous observations – in which the magnetization step disappears abruptly at  $T_{\varphi}$  replaced by a second magnetization peak below  $T_{\varphi}$  – our results show that when applying the AC field the magnetization step does not disappear but continues down to much lower temperatures instead of turning into a second magnetization peak. This suggests that the thermally induced FOT transition does not terminate at  $T_{\varphi}$  but continues far below it as a disorder-driven FOT. Showing that this prolongation of the FOT enters the disorder-driven regime supports this conclusion and excludes the possibility that the AC field's only effect was the extension of the thermally induced transition into lower temperatures. One of the ways to show this is to observe the shape of the melting line curve in the resulting  $B$ - $T$  phase diagram near  $T_{\varphi}$ . If the FOT revealed in Fig. 11b and 11c

were induced only by thermal fluctuations, the resulting melting curve would have continued rising towards higher fields with decreasing temperature because thermal fluctuations weaken as temperature decreases. Our results indicate otherwise, as explained below.

In order to derive the  $B$ - $T$  phase diagram, we need to determine accurately the field at which the transition occurs. For this the derivative of the magnetization with respect to the induction  $B_z$  in the vicinity of the transition was analyzed. Figure 12 shows the derivative of  $B_z - H_a$  with respect to  $B_z$ , as a function of  $B_z$ , at the temperature range between 44 K and 32 K, in the presence of the  $H_{ac}$ . The melting field  $B_m$  was determined as the peak of the Gaussian-like derivative curve, which is the value of the field at which the melting step has the highest slope. Using this procedure, we were able to map the transition line very accurately on the  $B$ - $T$  phase diagram.

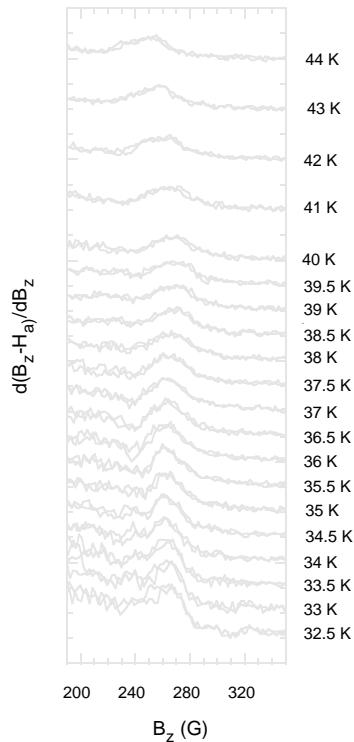


Fig. 12 A derivative of the magnetization  $B_z H_a$  with respect to  $B_z$  as a function of  $B_z$ . Every line corresponds to a different temperature in the temperature range, from 32.5 K to 44 K, as indicated on the right axis. The curves are vertically displaced for clarity.

Figure 13a shows a magnified view of the melting line on the  $B$ - $T$  phase diagram in the vicinity of the proposed  $T_q$ . The termination of the FOT line at 31 K indicates the lowest temperature below which we could not obtain reversible magnetization loops.

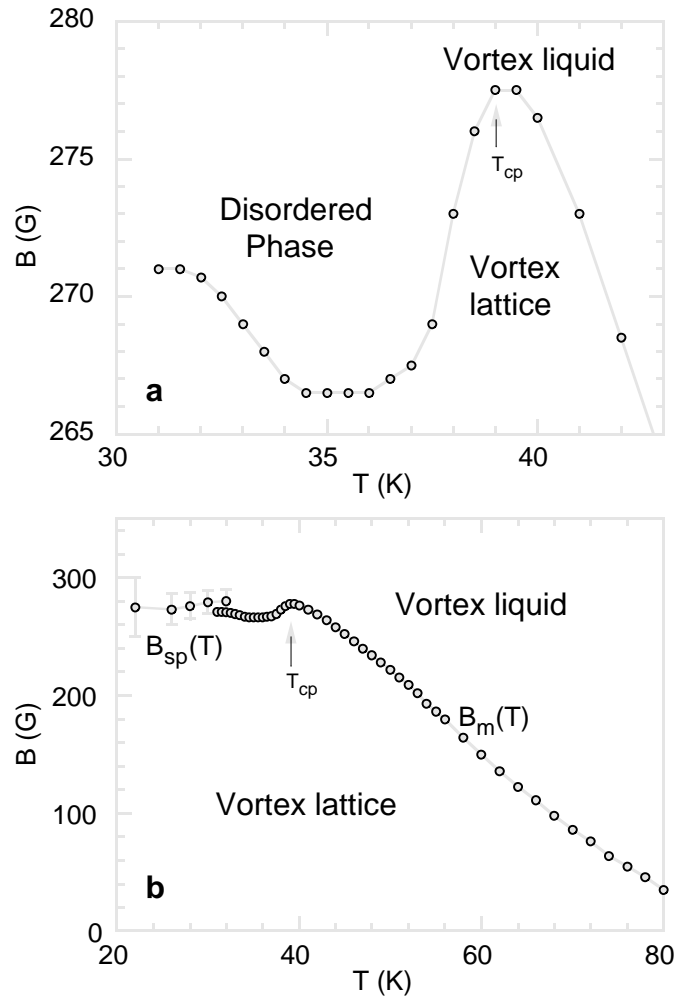


Fig. 13 (a) Magnified view of the melting line on a  $B$ - $T$  phase diagram in the vicinity of the critical point. At high temperatures, the vortex lattice transforms into a vortex liquid phase through a thermally induced FOT whereas at lower temperatures the vortex lattice transforms into a disordered vortex phase through a disorder-driven FOT transition. Below  $T_q$  the line shows a positive slope  $dB_m/dT$ , displaying an inverse melting behavior. (b) The entire melting transition  $B_m(T)$  along with the second peak transition  $B_{sp}(T)$  ( $\circ$ ).

The interesting observation in this figure is the shape of the FOT line. Notice that at  $T_q$  the slope of the melting curve changes sign: above this temperature, the melting line has a negative slope  $dB_m/dT$ , which characterizes the melting curve at high temperatures where

the FOT is governed by thermal fluctuations. Below this temperature, the melting line has a positive slope. This change in the curve direction cannot be induced by thermal fluctuations because thermal fluctuations weaken as temperature decreases, and as explained above – if the transition was induced only by thermal fluctuations, the melting curve would have continued rising towards higher fields as the temperature decreased. Thus, the change in the curve direction must be induced by material disorder and not by thermal fluctuations, i.e. *the extension of the FOT line beyond  $T_q$  is not just a matter of sensitivity but reveals a different FOT mechanism*

These results strongly suggest that the FOT line does not terminate at  $T_q$  but continues as a disorder-driven FOT at lower temperatures. Moreover, this extended FOT line coincides with the second peak transition line  $B_p(T)$ , as shown in Fig. 13b, which indicates that these two phenomena have a common origin – the reversible magnetization step is a thermodynamic signature of the transition, whereas the second magnetization peak is its dynamic characteristic reflecting the enhanced vortex pinning and slow dynamics in the disordered vortex phase. The revealed thermodynamic nature of the second peak transition is consistent with recent investigations based on the magneto optical imaging technique [44] and Josephson plasma resonance experiments [45]. In summary, these observations suggest that the melting transition and the second peak transition form a unified first-order transition that changes its character from a thermally induced transition to a disorder-driven one. Accordingly, the ordered lattice phase is always destroyed through a FOT, either the thermally induced FOT at high temperatures or the disorder-driven FOT at low temperatures.

### **Inverse Melting**

The shape of the FOT line, as shown in Fig. 13, reveals another important discovery. The region below  $T_q$  which is characterized by a positive slope, displays an unusual melting behavior. In contrast to the usual behavior where raising the temperature induces melting of a solid into a liquid, we observe an *inverse melting* process in which *heating* the vortex system induces transformation of a liquid or a *disordered* vortex phase into an *ordered* vortex lattice phase. This unexpected behavior was already found in polymeric systems [46,47] but was never previously observed in a vortex system. The thermodynamic nature of this inverse melting transition is apparently disorder-driven. This conclusion arises when trying

to understand the shape of the FOT line in Fig. 13 in terms of competition between the different energies. At low temperatures, where thermal fluctuations have a minor role, the transition is disorder-driven and should be rather temperature independent [36]. Such transition arises from the competition between the elastic energy of the lattice and the vortex pinning energy, where with increasing field the elastic energy of the lattice decreases relatively to the pinning energy, leading to a structural transition when the two energies become comparable [23]. At intermediate temperatures, the transition *remains* disorder-driven, but thermal fluctuations weaken the pinning effect of disorder and the pinning energy, resulting in an upturn in the transition line.

It should be emphasized that inverse melting does not violate the thermodynamic requirements of larger entropy in the higher temperature phase, but implies that the ordered vortex lattice has higher entropy than the disordered vortex phase. The entropy difference between the disordered vortex phase and the vortex lattice per unit volume can be calculated using the Clausius-Clapeyron relation,

$$\Delta S = -\frac{\Delta B}{4p} \frac{dH_m}{dT}$$

The entropy difference per vortex per CuO layer is therefore

$$\Delta s = -\frac{f_0 d}{B_m} \frac{\Delta B}{4p} \frac{dH_m}{dT}, \quad (d \text{ is the interlayer spacing}).$$

The measured height of the discontinuous step  $\Delta B$  and the associated  $\Delta s$  are shown in Fig. 14 as a function of the melting temperature  $T_m$ .  $\Delta B$  is rather constant in this range of temperatures. This observation resolves a previously reported inconsistency in the behavior near  $T_\varphi$  – at a true critical point,  $\Delta B$  is expected to decrease continuously to zero, whereas experimentally a rather constant  $\Delta B$  was found to disappear abruptly at  $T_\varphi$  [27]. This further suggests that  $T_\varphi$  is not a critical point, therefore  $\Delta B$  should not decrease to zero, and the previously reported disappearance of  $\Delta B$  at  $T_\varphi$  is an experimental limitation removed using the in-plane AC field.  $\Delta s$ , on the other hand, vanishes at  $T_\varphi$  because  $B_m(T)$  becomes horizontal when approaching  $T_\varphi$ . Below  $T_\varphi$   $\Delta s$  becomes negative, meaning that the entropy is higher in the ordered lattice phase than in the disordered vortex phase. The surprising conclusion, considering the notion that a higher degree of order implies a lower entropy, is that the lattice phase seems to be more disordered than the disordered vortex phase. Since the lattice is structurally more ordered as compared to the disordered phase,

which has a high concentration of dislocations, the extra entropy must arise from additional degrees of freedom. Therefore, even though there are no dislocations and the time averaged vortex positions retain a rather long-range order, the thermal fluctuations on short scales are larger in the ordered lattice as compared to the entangled disordered phase.

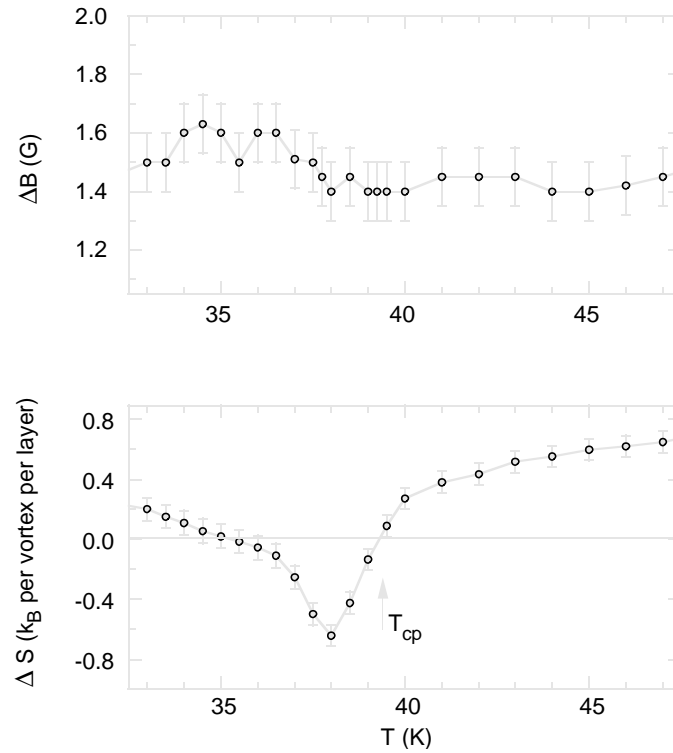


Fig. 14 The measured height of the discontinuous step  $\Delta B$  and the entropy difference  $\Delta S$  per vortex per CuO layer

It should be noted that  $\Delta B$  is relatively high compared to the step height that was measured at higher temperatures in this crystal. The  $H_{ac}$  was found to increase the height of the discontinuity, and this effect becomes more significant when raising the  $H_{ac}$  amplitude. This raises the question of whether  $H_{ac}$  field reveals the true height of the discontinuity, which was suppressed due to pinning, or whether it slightly distorts the true value of  $\Delta B$ . Further verification by additional methods is required in order to clarify this point.

## Chapter 6

### SUMMARY

The purpose of this work was to study the thermodynamic nature of the vortex matter phase transitions in the low temperature region of the phase diagram. In particular, we have investigated the termination of the melting line at a critical point, the behavior of the melting line in the vicinity of the critical point, and the thermodynamic nature of the second peak transition. The local Hall sensors technique, combined with the in-plane AC magnetic field, were utilized for this purpose. The application of the AC field enabled the observation of the vortex properties close to equilibrium conditions, which revealed new phenomena.

The material of choice for these measurements was  $\text{Bi}_2\text{Sr}_2\text{CaCu}_2\text{O}_8$ . The initial measurements have shown that in BSCCO crystals, the application of a transverse AC field fully suppresses the magnetic hysteresis at low temperatures and allows the extension of the reversible regime in the  $H$ - $T$  phase diagram to lower temperatures.

Further measurements have revealed a thermodynamic evidence of a FOT along the second magnetization peak line, at temperatures below  $T_\varphi$ . The measurements have shown that the FOT line does not terminate at  $T_\varphi$  but continues down to at least 30K. This implies that  $T_\varphi$  is not a real critical point, and the previously reported termination of the melting line at  $T_\varphi$  only reflects an experimental limitation.

Detailed mapping of the transition lines on a  $B$ - $T$  phase diagram has shown that this FOT changes its direction at  $T_\varphi$  and coincides with the second peak transition at low temperatures. These observations imply that the second peak transition is a first-order transition. Accordingly, the ordered vortex lattice phase is always destroyed through a unified first-order transition that changes its character from a thermal melting transition to a disorder induced one.

The last finding was that at intermediate temperatures this transition shows an inverse melting behavior in which the disordered vortex phase transforms into an ordered lattice phase when increasing the temperature.

## REFERENCES

1. G. Bednorz and K.A. Müller, Z. Phys. B, **64**, 189 (1986).
2. G. Blatter *et al.*, Rev. Mod. Phys. **66**, 1125 (1994).
3. D. Majer, E. Zeldov, H. Shtrikman and M. Konczykowski, in “Coherence in High Temperature Superconductors”, edited by G. Deutscher and A. Revcolevschi, World Scientific (Singapore), 1996.
4. D. Majer, Ph.D. Thesis, Weizmann Institute of Science, Rehovot, Israel (1997).
5. M. Willemin, C. Rossel, J. Hofer and H. Keller, A. Erb and E. Walker, Phys.Rev.B **58**, R5940 (1998).
6. L. Forro. Phys. Letters A **179**, 140 (1993).
7. H. Kamerlingh Onnes, Leiden Comm. **120b**, **122b**, **124c** (1911).
8. W. Meissner and R. Ochsenfeld, Naturwissenschaften **21**, 787 (1933).
9. M. Tinkham, Introduction to Superconductivity, McGraw-Hill, Chapter 4 (1996).
10. V.L. Ginzburg and L.D. Landau, Zh. Eksp. Teor. Fiz, **20**, 1064 (1950).
11. P.G. de Gennes, Superconductivity of Metals and Alloys, Addison-Wesley Publishing Co.,Chapter 6 (1966).
12. A.A. Abrikosov, Fundamental of the Theory of Metals, North Holland (1988).
13. A.A. Abrikosov, JETP, **5**, 1174-1182 (1957).
14. U. Essman and H. Traeuble, Phys. Lett. A, **24**, 526 (1967).
15. D. Cribier, B. Jarcot, L. Madhav Rao and B. Farnoux, Phys. Lett. **9**, 106 H. W. Weber, J. Scheller, and G. Lippman, Phys. Status Solidi (b), **57**, 515 (1973). (1968).
16. H. W. Weber, J. Scheller, and G. Lippman, Phys. Status Solidi (b), **57**, 515 (1973).
17. J. Bosch, R. Gross, M. Koyanagi and R.P Huebener, Phys. Rev. Lett. **54**, 1448 (1985).
18. T. Matsuda, S. Hasegawa, M. Igarashi, T. Kobayashi, M. Naito, H. Kajiyama, H. Endo, N. Osakabe, A. Tomomura and R. Auki, Phys. Rev. Lett. **62**, 2519 (1989).
19. A. M. Change, H.D. Hallen, H.F. Hess, H.L. Kao, J. Kwo, A. Sudbo and T. Y. Chang, Europhys. Lett. **20**, 645, (1992).
20. M. Tinkham, Introduction to Superconductivity, McGraw-Hill, Chapter 5 (1996).
21. B. Oh *et al.*, Phys. Rev. B **37**, 7861 (1988).
22. D.R. Nelson, Phys. Rev. Lett. **60**, 1973 (1988).
23. V. Vinokur, B. Khaykovich, E. Zeldov, M. Konczykowski, R.A. Doyle, P. H. Kes, Physica C **259**, 209 (1998).
24. E. Brézin, D.R. Nelson, A. Thiaville, Phys. Rev. B **31**, 7124 (1985).
25. H. Safar, P.L. Gammel, D.H. Huse, D.J. Bishop, J.P. Rice, Phys. Rev. Lett. **69**, 824 (1992)
26. D.T. Fuchs, E. Zeldov, D. Majer, R.A. Doyle, T. Tamegai, S. Ooi, M. Konczykowski, Phys. Rev. B **54**, R796 (1996).
27. E. Zeldov, D. Majer, M. Konczykowski, V. B. Geshkenbein, V. M. Vinokur and H. Shtrikman, Nature (London) **375**, 373 (1995).
28. R.A Doyle, D. Liney, W.S. Seow, A.M. Campbell, Phys. Rev. Lett. **75**, 4520 (1995).
29. A. Schilling *et al.*, Nature (London) **382**, 791 (1996).
30. M. P. A. Fisher, Phys. Rev. Lett. **62**, 1415 (1989).
31. R. Cubitt *et al.*, Nature (London) **365**, 407 (1993).
32. B. Khaykovich *et al.*, Phys. Rev. Lett. **76**, 2555 (1996).
33. B. Khaykovich *et al.*, Phys. Rev. B **56**, R517 (1997).

34. T. Giamarchi and P. Le Doussal, Phys. Rev. B **52**, 1242 (1995).
35. C.P. Bean, Phys. Rev. Lett. **8**, 250 (1962).
36. D. Etras and D.R. Nelson, Physica C **79**, 272 (1996).
37. R. Cubitt *et al.*, Physica **235C-240C**, 2583 (1994).
38. T.W. Li, P.H. Kes, N.T. Hien, J.J.M. Franse and A.A. Menovsky, J. Crystal Growth **135**, 481 (1994).
39. S. Ooi., T. Shibauchi, T. Tamegai, Physica C **302**, 339 (1998).
40. A.E. Koshelev, Phys. Rev. Lett. **83**, 178 (1999).
41. C.P. Bean and J.D. Livingston, Phys. Rev. Lett. **12**, 14 (1964).
42. E. Zeldov *et al.*, Phys. Rev. Lett. **73**, 1428 (1994).
43. B. Schmidt and M. Konczykowski, N. Morozov and E.Zeldov, Phys. Rev. B **55**, R8705 (1994).
44. C.J. Van der Beek, S. Colson, M.V. Indenbom, and M. Konczykowski, Phys. Rev. Lett. **84**, 4196 (2000).
45. M.B. Gaifullin, Y. Matsuda, N. Chikumoto, J. Shimoyama, and K. Kishio, Phys. Rev. Lett. **84**, 2945 (2000).
46. A.L. Greer, Nature **404**, 134 (2000).
47. S. Rastogi, G.W.H. Hhne and A. Keller, Macromolecules **32**, 8897 (1999).